Check for updates

Systematic analysis of reaction parameters driving the hydrothermal growth of layered VS$_2$†

H. K. Shahzad, [iD] *[a] Zhengri Huang, [iD] [a] Sasan Ghashghaie, [iD] [a] Han Liu, [iD] [a] G. Muhyodin,[a] Mohsen Tamtaji, [iD] [b] Hoi Lam Li,[a] F. Chuan Chan[a] and C. Y. Chung [iD] *[a]

Two-dimensional metallic vanadium disulfide (VS$_2$) has gained significant attention due to its excellent electrical and electrochemical properties, making it a promising candidate for energy storage and electronic applications. Despite the advantages of hydrothermal synthesis in producing VS$_2$ nanosheets, the underlying reaction pathways and critical synthesis parameters remain insufficiently understood. This study presents a systematic investigation of the key reaction variables influencing the hydrothermal growth of hierarchical VS$_2$ nanosheets on a three-dimensional substrate. By optimizing precursors' (NH$_4$VO$_3$: TAA) molar ratios, reaction temperature, time, and ammonia concentration, we achieved precise control over the morphology and phase of VS$_2$. Our findings demonstrate that pure VS$_2$ nanosheets can be synthesized in just 5 hours, significantly reducing the conventional reaction time of 20 hours while maintaining phase purity and structural integrity. The parametric insights provided in this study establish a robust foundation for designing tunable VS$_2$ architectures with potential applications in catalysis, sensors, hydrogen evolution, and next-generation energy storage devices.

1. Introduction

The manipulation of nanostructures offers transformative potential across various applications due to their unique physical, chemical, and electrochemical properties. Transitioning from microstructures to nanostructures dramatically increases the interfacial area, which can significantly enhance electrochemical performance. Precision control over the size, shape, and composition of these nanostructures is crucial for optimizing their use in cutting-edge technologies.[1–6]

Vanadium disulfide (VS$_2$), a two-dimensional (2D) transition metal dichalcogenide (TMD), has attracted significant attention due to its remarkable electrical, electrochemical, and catalytic properties.[7–12] These characteristics make VS$_2$ a strong candidate for applications in next-generation energy storage devices, catalysis, and hydrogen evolution reactions (HER).[13–17] However, despite its potential, achieving high-quality VS$_2$ with precise control over its structure and properties remains challenging.

Historically, several methods have been employed for the synthesis of VS$_2$, ranging from chemical vapor deposition (CVD) to solution-based techniques. Among these, the hydrothermal method has emerged as a particularly attractive route due to its simplicity, cost-effectiveness, and scalability.[18–20] While early work in VS$_2$ synthesis primarily focused on bulk materials, recent advancements in hydrothermal techniques have enabled better control over the morphology of the material, allowing for the formation of nanosheets, hierarchical structures, and flower-like morphologies. Despite these advancements, the underlying mechanisms driving VS$_2$ nucleation and growth, particularly under hydrothermal conditions, are still not fully understood.

The challenges in VS$_2$ synthesis are multifaceted, including control over phase purity, crystallinity, and morphology.[21,22] The ability to tune these characteristics is crucial, as they directly influence the performance of the material in applications such as batteries and catalysts. In particular, the morphology of VS$_2$ can significantly affect its electrochemical behavior. Yet, the precise role of reaction parameters such as temperature, precursor ratios, and reaction time in controlling this morphology has been inadequately explored. Previous studies on the hydrothermal growth of VS$_2$ have provided valuable information but often lack a systematic investigation of how specific reaction parameters influence the nucleation and growth processes.

The present study addresses this gap by conducting a detailed parametric optimization of VS$_2$ nanostructures

[a] Department of Materials Science and Engineering, City University of Hong Kong, Kowloon Tong, Hong Kong SAR, China. E-mail: hkshahzad2-c@my.cityu.edu.hk
[b] Department of Chemical and Biological Engineering, The Hong Kong University of Science and Technology, Clear Water Bay, Kowloon, Hong Kong, China

† Electronic supplementary information (ESI) available. See DOI: https://doi.org/10.1039/d4ce01161a

synthesized *via* hydrothermal processes. Using scanning electron microscopy (SEM) and X-ray diffraction (XRD), we investigate how variables such as reaction time, temperature, precursor molar ratios, and ammonia concentration influence the growth of two-dimensional VS_2 on a three-dimensional framework. This research is expected to provide valuable insights into the synthesis and optimization of VS_2 nanomaterials, potentially informing future advancements in nanotechnology and related fields.

2. Experimental

2.1 Direct growth and characterization of VS_2 nanosheets on a stainless-steel mesh substrate

A three-dimensional porous sponge-like self-standing architecture of flower-like VS_2 was constructed on a flexible 316 L stainless-steel (SS) substrate (300 mesh). The SS mesh was selected for its large surface area compared to a flat substrate, facilitating lateral growth of freestanding nanosheets. Additionally, it is cost-effective and readily available.

2.2 Hydrothermal synthesis procedure

Four different molar ratios of the initial precursors (NH_4VO_3 and TAA) were investigated: 1:2.5, 1:5, 1:7.5, and 3:5. These were mixed with varying amounts of ammonia solution (2–6 mL) in 30 mL of deionized water. The mixture was magnetically stirred for 1 hour at room temperature to obtain a homogeneous black solution, indicating complete dissolution of NH_4VO_3. The homogeneous black solution, along with a rectangular piece of SS mesh (1.8×4.8 cm^2), were transferred into a 50 mL Teflon-lined stainless-steel autoclave. The autoclave was sealed and heated to different reaction temperatures (100 °C, 140 °C, 180 °C, and 220 °C) for various holding times (≤ 1, 2, 3, 5, 10, and 20 hours) to synthesize VS_2. After cooling, the mesh was recovered, revealing freestanding VS_2 flakes grown on the SS mesh (VS_2/SS). The mesh was thoroughly washed with deionized water and ethanol multiple times and dried in a vacuum oven at 60 °C for 12 hours. The detailed synthesis parameters are summarized in Table 1.

2.3 Characterization techniques

X-ray Diffraction (XRD): the crystal structures of the samples were studied using a Rigaku Smart-Lab SE and BRUKER SRD-D2 Phaser diffractometers with a Cu Kα radiation source ($\lambda = 1.54184$ Å).[23,24] Morphological Analysis: Field emission scanning electron microscopy (FE-SEM) was performed using a Philips XL30 ESEM-FEG and a JEOL-820 SEM.[25] This analysis provided morphological data, energy dispersive spectra (EDS), and elemental mapping. XRD and SEM analyses enabled the investigation of transitions in crystal structures and morphologies of VS_2 as a function of various processing parameters.

2.4 DFT calculations

We carried out density functional theory (DFT) calculations to calculate the interlayer distancing of VS_2 to elucidate the effect of ammonia, which is generated during TAA decomposition, on the interlayer spacing of VS_2. We applied spin-polarized DFT calculations in the Vienna *ab initio* simulation package (VASP 6.1.0).[26] The Perdew–Burke–Ernzerhof (PBE) functional, along with a plane-wave cutoff energy of 500 eV, was employed, and the VASPsol package was used to incorporate implicit solvation (water).[27] DFT-D3 method was used to consider Van der Waals dispersion interactions.[26,28] As shown in Fig. 9, 3×3 supercell of the VS_2 (9.56 Å × 9.56 Å) were constructed, and a vacuum space of 30 Å in the *z* direction was applied to avoid interactions between periodic images. Monkhorst–Pack scheme with a $3 \times 3 \times 1$ *k*-point grid was utilized for structural relaxation. The convergence criteria for the electronic structure energy and force on each atom were set to be 10^{-6} eV and 0.02 eV Å^{-1}, respectively.[26]

3. Optimization of reaction parameters to synthesize layered VS_2

The analysis began with exploring preexisting literature on the hydrothermal synthesis of VS_2 crystals, identifying crucial parameters, as listed in Table S1.† It was observed that the parameters used by various researchers to produce layered VS_2 nanosheets (NSs) were inconsistent. This study aims to analyze the inconsistencies in these synthesis parameters. A radar chart was created, plotting five parameters (volume, precursor molar ratio, amount of ammonia, reaction temperature, and time) along the axes to form a pentagon (Fig. 1a). Six different studies from Table S1† (highlighted in blue) are represented on the radar chart with different color shades. To clearly illustrate the parametric inconsistencies, these overlapping graphs were further split into six separate pentagonal plots (Fig. 1b).

For instance, Zhu *et al.*[29] employed a 1:10 initial precursor molar ratio (PMR) in 30 mL of solvent with a 6 mL

Table 1 Hydrothermal reaction variables employed for the VS_2 growth

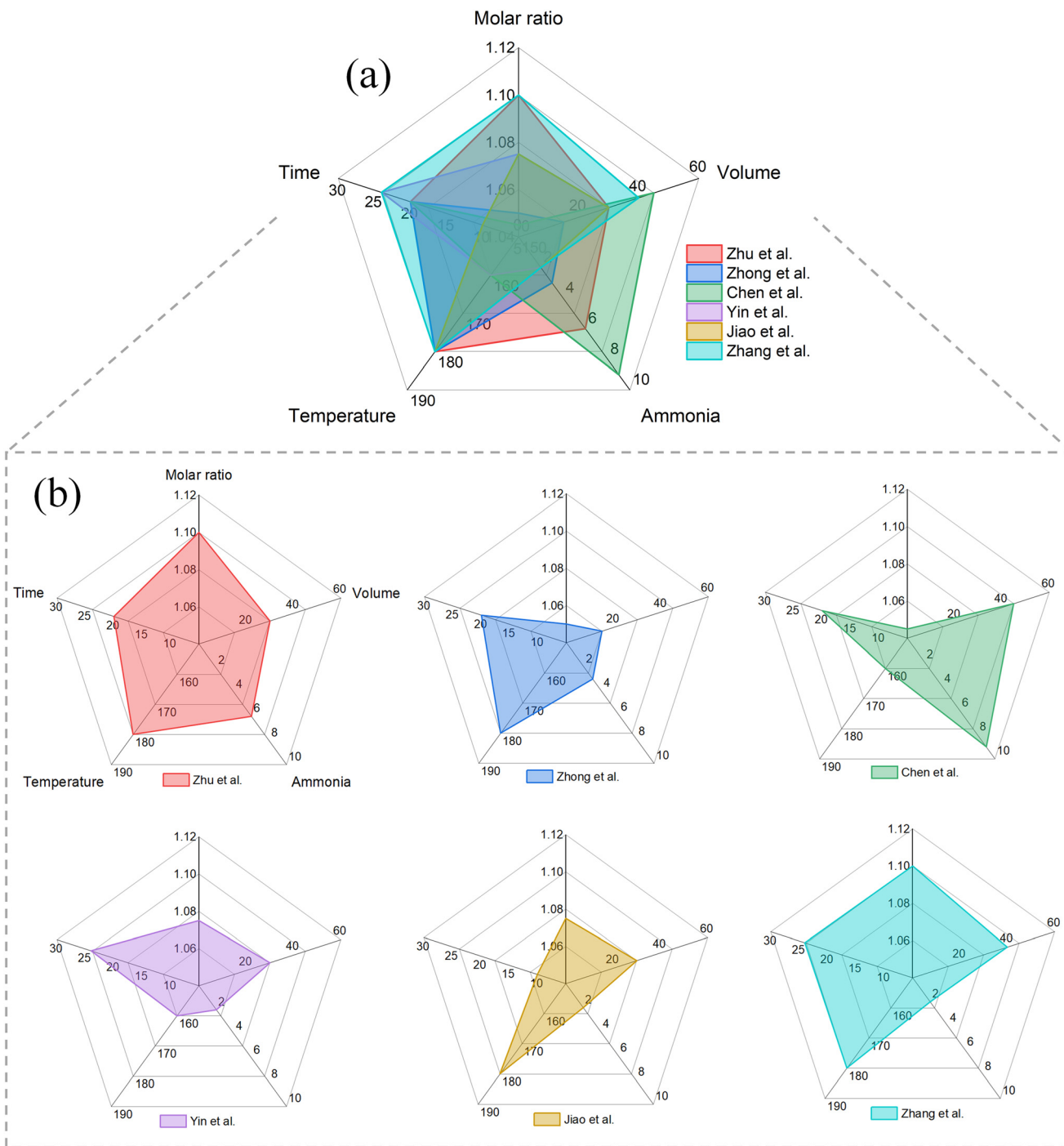| Volume (mL)	Precursor molar ratio (NH_4VO_3 : TAA)	Precursor concentration (multiplying factor)	Temperature (°C)	Reaction time (hours)	Ammonia concentration (mL)
30	1:2.5 (mmol)	2 × 15	100	≤1	0
30	1:5 (mmol)	3 × 22.5	140	5	2
30	1:7.5 (mmol)	4 × 30	180	10	4
30	3:5 (mmol)	5 × 37.5	220	15	6
30	—	6 × 45	—	20	—

Fig. 1 (a) Radar chart showing the reaction variables used in the literature: molar ratio (%), volume (mL), amount of ammonia (mL), reaction temperature (°C), and time (hours). (b) Expansion of Fig. 1a to represent the individual study.

ammonia concentration. In contrast, Zhang et al.[30] used a 1 : 10 PMR with 2 mL of NH₃ in 40 mL of solvent. Zhong et al.[31] reduced the PMR to 1 : 5 and the solvent volume to 15 mL, with 3 mL of NH₃. Meanwhile, Chen et al.[32] used a lower molar ratio of 1 : 5 in a larger solvent volume of 45 mL, with 9 mL of NH₃.

Most of the reported research used 30 mL of solution in a 50 mL container (Table S1†). For consistency and easy

comparison with previous studies, 50 mL Teflon-lined autoclaves were employed in this investigation. A piece of stainless-steel mesh (1.8×4.8 cm²) was inserted into the container with 30 mL of the homogeneous mixture, ensuring the SS mesh was completely immersed as a substrate for growing VS₂. It is essential to ensure the SS mesh is fully submerged in the solution to facilitate uniform deposition. This study aimed to examine how various processing

variables, such as the molar ratio of the starting precursors, their concentrations, reaction temperature, reaction time, and the amount of ammonia, influence the deposition of VS_2 on the SS mesh, as listed in Table 1.

3.1 Effect of precursors' molar ratio

The analysis began by investigating the effect of molar ratios of the initial precursors (NH_4VO_3 and TAA) on the formation process of VS_2 nanosheets, as described in Table 1. The masses of NH_4VO_3 and TAA were calculated in millimoles (mmol). The molecular weight of NH_4VO_3 is ~117 g mol^{-1} (NH_4VO_3: 14 + 4(1) + 51 + 3(16) = ~117 g mol^{-1}), and the molecular weight of TAA ($C_2H_3SNH_2$) is ~75 g mol^{-1} ($C_2H_3SNH_2$: 2(12) + 3(1) + 32 + 14 + 2(1) = ~75 g mol^{-1}). Therefore, 1 mmol of NH_4VO_3 corresponds to 0.117 g and 1 mmol of TAA to 0.075 g.

All other processing parameters were fixed based on the most frequently used ones from Table S1:† temperature = 180 °C, reaction time = 20 hours, and ammonia solution (NH_3) = 2 mL. In addition to the molar ratio, the quantity or concentration of the precursors also significantly impacts the final yield. In this study, the amount of the precursors used was five times (5×) their molar ratio.

Fig. 2(a–d) presents SEM images of four samples prepared with different molar ratios (1 : 2.5, 1 : 5, 1 : 7.5, and 3 : 5). The 1 : 2.5 sample (in which 1 mmol of NH_4VO_3 (corresponding to 1 × 0.117 g) was combined with 2.5 mmol of TAA (2.5 × 0.075 g)), represents a lower TAA concentration compared to prior studies (see Table S1†). This ratio exhibited a mixed morphology of flake-like VS_2 nanosheets and granular particles, as seen in SEM images (Fig. 2a). These granules ranged from 1 to 5 μm in diameter, dispersed in the interstitial

spaces of the mesh. XRD analysis (green pattern in Fig. 3) confirmed the presence of VS_2, with characteristic peaks matching JCPDS no. 89-1640. However, a noticeable reduction in the (001) peak intensity was observed, suggesting a deviation from the well-ordered layered structure typically associated with VS_2. Simultaneously, a minor peak corresponding to vanadium oxide appeared at $2\theta = 42°$ (denoted by an asterisk), indicating the formation of secondary oxide phases at this molar ratio. EDX analysis (Fig. S1a†) revealed a V : S atomic ratio of approximately 1 : 2 in the nanosheet-like regions, consistent with VS_2 stoichiometry, while the granular structures exhibited a vanadium-rich composition.

Increasing the TAA concentration to 5 mmol and 7.5 mmol (1 : 5 and 1 : 7.5 ratios) resulted in a significant morphological transformation, with the emergence of uniform, flower-like VS_2 nanosheets (Fig. 2b and c). The absence of whitish granules in these samples indicates that higher TAA concentrations favor the formation of well-defined layered VS_2 structures. Correspondingly, XRD patterns (red and magenta lines in Fig. 3) exhibited enhanced (001) peak intensity, reinforcing the association between TAA concentration and layered morphology.

To further assess the effect of NH_4VO_3 concentration, we synthesized a 3 : 5 sample, maintaining the TAA concentration at 5 mmol while increasing NH_4VO_3 to 3 mmol. As shown in Fig. 2d, this sample predominantly comprised agglomerated, dense granules with minimal presence of well-defined nanosheets. High-resolution SEM images (Fig. S1b†) revealed thin, hair-like flakes within these granules, along with randomly oriented, square-shaped crystalline structures. EDX analysis confirmed that these structures were vanadium-rich, and XRD analysis (blue
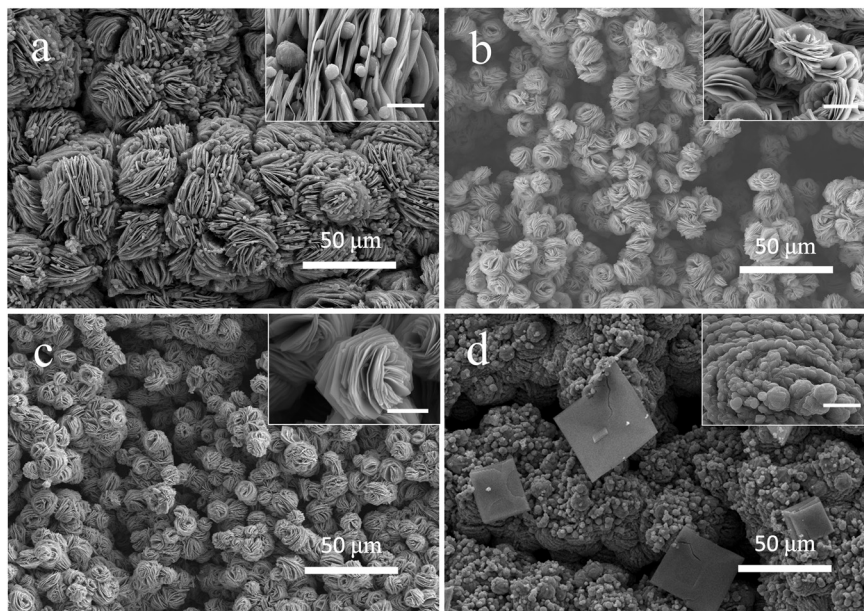

Fig. 2 SEM micrographs of VS_2/SS prepared with different molar ratios of NH_4VO_3 : TAA (a) 1 : 2.5 (b) 1 : 5 (c) 1 : 7.5 (d) 3 : 5 (the scale bar in the inset images is 5 μm).
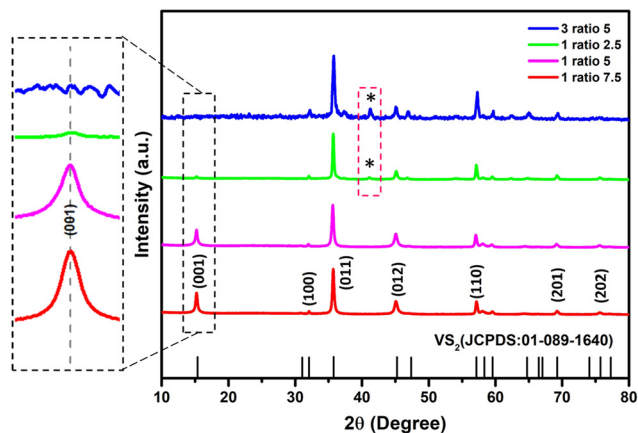
Fig. 3 XRD patterns of VS$_2$/SS prepared with different molar ratios of NH$_4$VO$_3$: TAA.

pattern in Fig. 3) provided further insights into their composition. The (001) peak was absent in the 3 : 5 sample, confirming a complete suppression of the layered VS$_2$ phase, while the vanadium oxide peak at $2\theta = 42°$ became more pronounced.[33] These results indicate that an excess of NH$_4$-VO$_3$ disrupts the formation of VS$_2$ nanosheets and instead promotes the precipitation of vanadium-rich phases.

In summary, our findings highlight the critical role of precursor molar ratios in tailoring VS$_2$ morphology and crystallinity. Higher TAA concentrations promote the formation of well-defined layered VS$_2$, as evidenced by the pronounced (001) peak. In contrast, higher NH$_4$VO$_3$ concentrations lead to granular morphologies, dwindled (001) peak intensity, and the emergence of vanadium oxide phases. While conventional XRD provides insight into phase evolution, advanced techniques such as XRD pole figure analysis would be required to fully resolve the preferential orientation and interlayer characteristics of VS$_2$ synthesized under different precursor conditions.[34]

3.2 Effect of precursors' mass loading

The mass loading of the preliminary precursors (NH$_4$VO$_3$: TAA) determines the final yield of VS$_2$ on the substrate. This study investigated the effect of varying the precursor mass loading while maintaining a constant molar ratio of NH$_4$VO$_3$ to TAA (1 mmol : 7.5 mmol). The mass loading was adjusted by multiplying this ratio by a integer (multiplying factor). For example, to increase the mass loading fourfold (4×), the ratio 1 : 7.5 was scaled to 4 : 30. This experiment explored five different mass loadings (from 2× to 6×), as detailed in Table 1. All samples were heated at 180 °C for 20 hours, with the ammonia concentration fixed at 2 ml.

As shown in Fig. 4a, increasing the precursor mass loading from 2× to 6× resulted in a steady increase in VS$_2$ yield on the SS-mesh substrate, following a near-linear trend. At a 2× loading (2 mmol : 15 mmol), the VS$_2$ yield was 8.8 mg cm^{-2}, increasing to 14.5 mg cm^{-2} for 3× loading (3 mmol : 22.5 mmol). Further increases to 4× and 5× loadings led to yields of 18.7 mg cm^{-2} and 24.2 mg cm^{-2}, respectively. Beyond 6× loading, the VS$_2$ layer became excessively thick, leading to potential mechanical instability during handling.

To compare this single-step hydrothermal approach with a repeated hydrothermal method,[35] we conducted additional rounds of synthesis using the same precursor molar ratio (1 : 7.5) and a concentration of 2× for each round. The results in Fig. 4b show that the repeated hydrothermal reaction also follows a linear yield increase. Interestingly, in the second round of synthesis, the yield approached values similar to those achieved using 6× precursor loading in a single step. This suggests that while repeated hydrothermal rounds can produce high yields with lower precursor amounts per step (1 : 7.5 mmol × 2), the single-step process significantly reduces synthesis time by achieving comparable yields in a single reaction cycle.

Given the balance between yield efficiency and material stability, we selected the 3× precursor loading (highlighted in green in Fig. 4a) as the optimal condition for subsequent experiments. This loading was deemed sufficient for ensuring structural integrity while maintaining a high VS$_2$ yield for our cathode preparation. Detailed electrochemical performance will be discussed in a subsequent study. For further insights into the
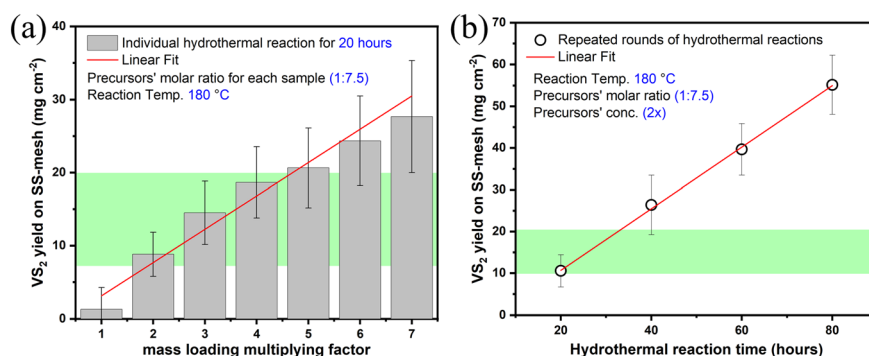

Fig. 4 (a) Bar chart displaying the effect of initial precursors' (NH$_4$VO$_3$: TAA) mass loadings (each bar has fix molar ratio of 1 : 7.5 times multiplying factor) on the VS$_2$ yield after a single-step hydrothermal process for 20 hours of reaction time. (b) Scattered chart of a sample (1 : 7.5 mmol × 2) showing the effect of repeated rounds of hydrothermal reactions, of 20 hours each, on the VS$_2$ yield.

morphological evolution associated with increasing precursor mass loading, refer to Fig. S2 in the ESI.†

3.3 Effect of reaction temperature

In light of the aforementioned experimental observations, we fixed the precursors' molar ratio at 1 : 7.5 and concentrations at 3× for further investigation. In the next stage, we examined the impact of reaction temperature on the synthesis of VS_2 nanosheets using SEM and XRD analyses. Fig. 5(a–d) presents the SEM images of VS_2 morphologies obtained at different heating temperatures: 100 °C, 140 °C, 180 °C, and 220 °C, respectively. All samples (VS_2/SS) contained 2 mL of the ammonia solution and were heated for 20 hours.

At 100 °C, the morphology was characterized by micro-spherical bead-like structures, emerging from a homogeneous layer that covered the individual wires of the SS mesh. Each bead measured approximately 5–8 μm and consisted of loosely stacked false sheets or plate-like

structures, suggesting an incomplete crystallization process at this temperature. However, XRD analysis confirmed that the phase at this temperature was not pure VS_2 (Fig. 5e), further supporting the observation that insufficient thermal energy hindered the nucleation and growth of well-defined VS_2 nanosheets.

As the reaction temperature increased to 140 °C, 180 °C, and 220 °C, morphology evolved into a highly hierarchical framework of hexagonal micro-flowers (Fig. 5b–d). These lamellar structures comprised an interconnected network of 2D nanosheets, with each micro-flower consisting of curved, ultrathin flakes oriented at various angles, resembling blooming petals. The morphology was consistent across this temperature range and similar to those observed in the 1 : 5 and 1 : 7.5 molar ratio samples (Fig. 2b and c), demonstrating the temperature-induced growth of well-ordered VS_2 crystals. The XRD patterns confirmed that these phases were pure VS_2, with all peaks well-indexed to JCPDS database no. 89–1640 (Fig. 5e), implying that higher reaction temperatures
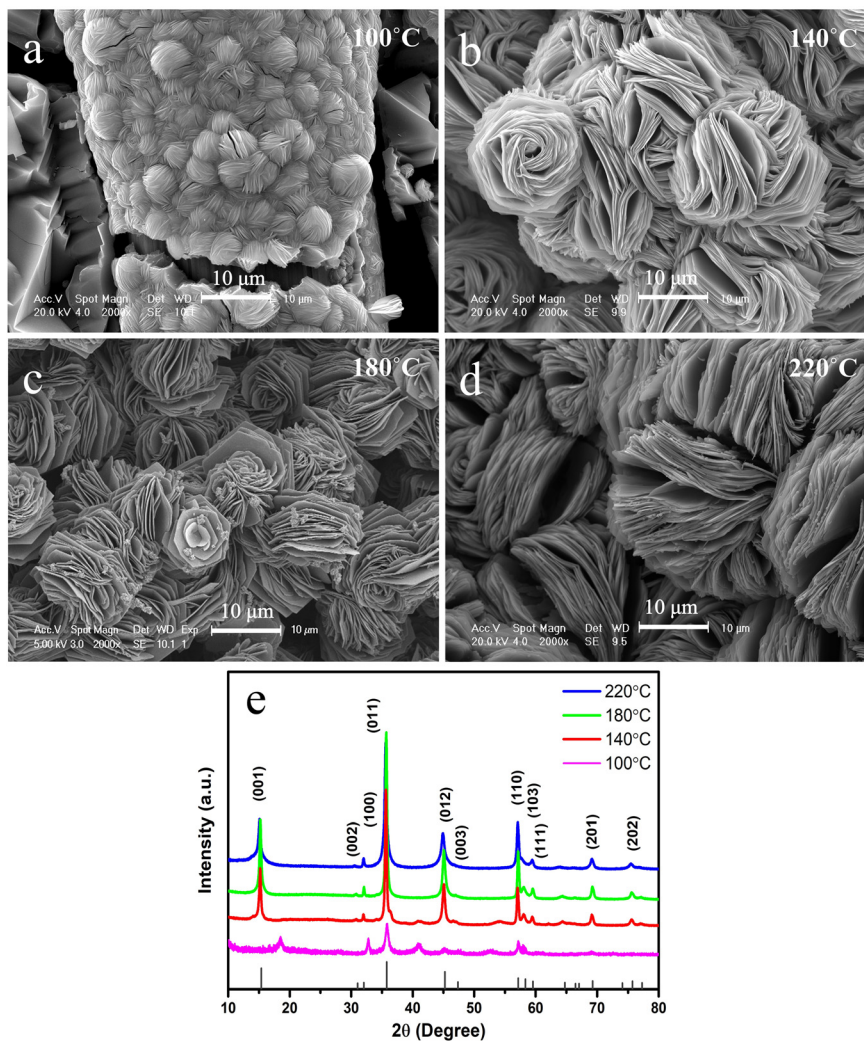

Fig. 5 (a–d) SEM images and (e) XRD patterns of VS_2/SS samples synthesized at different reaction temperatures of 100 °C, 140 °C, 180 °C, and 220 °C for 20 hours of heating time. The molar ratio of NH_4VO_3 and TAA was 1 : 7.5 in mmol, while their mass loading was 3×.

facilitated enhanced crystallization and structural order. Furthermore, the hierarchical architecture observed at this temperature range is advantageous for applications requiring high surface area and ion accessibility. The consistent presence of highly ordered VS_2 nanosheets within this temperature range suggests that the nucleation and growth processes are optimized between 140 °C and 220 °C, preventing excessive aggregation or disorder.

Our experiments indicate that flower-like VS_2 structures can be synthesized on a substrate within a temperature range of 140–220 °C *via* a hydrothermal process, provided careful attention is given to the molar ratios of the preliminary precursors. Among the tested temperatures, 180 °C was selected for further experiments, as it yielded well-defined hierarchical microstructures with high crystallinity and uniform nanosheet formation. Furthermore, an extensive review of the literature (Table S1†) confirms that 180 °C has been widely employed in previous hydrothermal syntheses of VS_2, supporting its suitability as an optimal reaction temperature.

3.4 Effect of reaction time

Our prior investigation enabled the optimization of three key reaction variables (reaction temperature, precursors' molar ratio, and mass loading) for synthesizing VS_2 *via* the hydrothermal method. To further understand the morphological evolution of VS_2 growth, we conducted time-dependent reaction experiments. Intermediate products at various stages were collected and analyzed using SEM, EDX, and XRD.

Fig. 6(a–d) shows the SEM images of samples prepared at reaction times of 1, 5, 10, and 20 hours. After 1 hour, microspheres with yarn-ball-like morphology and diameters of approximately 10 μm were observed. These densely packed balls were composed of fused circular nanoflakes resembling threads (Fig. 6a). XRD analysis suggested that this yarn-ball-like phase was not pure VS_2 at this early stage of the reaction (Fig. S4a†).

The yarn-ball-like microspheres began to transform as the reaction progressed to 5 hours. The structures appeared to open up, allowing individual nanosheets to be distinguished, although no significant change in the overall size of the spheres was observed. The individual flowers were fully developed, consisting of hexagonal nanosheets. Additionally, the space between the nanoflakes expanded, transforming the microspheres into blooming flowers composed of lamellar nanosheets (Fig. 6b). Variations in VS_2 crystal shape, from irregular to hexagonal, have been observed previously.[36] The XRD pattern of the sample at 5 hours confirmed the formation of pure VS_2, indicating that pure VS_2 was synthesized by this time (Fig. S4a†). Interestingly, no significant differences in size or morphology were detected between the 10-hour and 20-hour samples (Fig. 6c and d) also, suggesting that the flower-like morphology of the VS_2 phase was established by 5 hours of reaction time. The diffraction peaks of these samples were sharp, indicating good crystalline quality, and matched perfectly with the standard VS_2 phase (JCPDS no. 89-1640).

To better understand the formation mechanism of VS_2, we conducted time-resolved hydrothermal reactions and interrupted the process at 15-minutes, 30-minutes, and 45-minutes intervals (Fig. S4b†). In the first 15 minutes, two distinct intermediate phases were observed: large dendritic vanadium-oxide-based crystals (≤1 mm) and an amorphous sulfur-rich phase surrounding the SS mesh (Fig. 7a and b). These intermediates were confirmed not to be pure VS_2 through EDX and XRD analyses (Fig. S5a and b†).
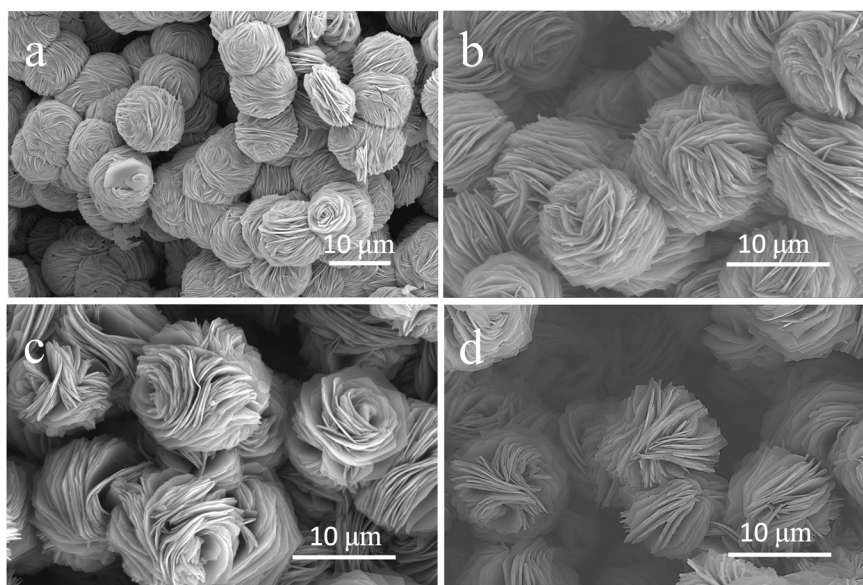

Fig. 6 (a–d) SEM images showing microstructural evolution with different hydrothermal reaction times of 1, 5, 10, and 20 hours, respectively.
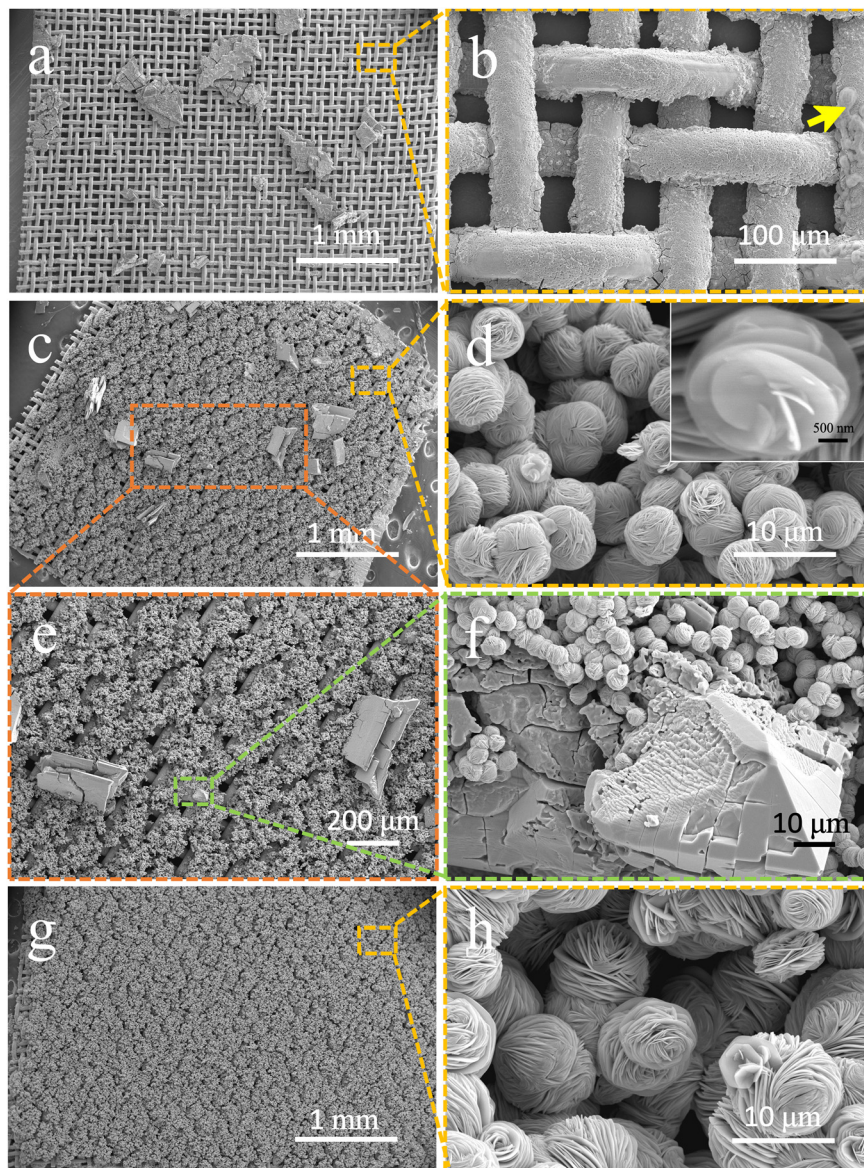
Fig. 7 SEM micrographs of VS$_2$/SS samples prepared at (a and b) 15 min, (c–f) 30 min, and (g and h) 45 min of hydrothermal reaction times.

Additionally, a translucent phase, marked by an arrow in the zoomed image (Fig. 7b), was found surrounding the SS mesh. This phase was sulfur-rich according to the EDX analysis (Fig. S5b†).

After 30 minutes (Fig. 7c), VS$_2$ microspheres (~4–6 µm) began to form, composed of circular nanosheets, as evidenced in Fig. 7d. This indicates that nucleation and crystal growth occurred between 15 and 30 minutes. Interestingly, the dendritic vanadium-oxide crystals appeared to dissolve during this stage, contributing to the formation of VS$_2$ microspheres, which reduced in size by nearly half compared to the 15-minute sample (Fig. 7e). At the 45-minute mark, the dendrites had completely disappeared, leaving only larger microspheres (8–10 µm) formed by further growth between 30 and 45 minutes (Fig. 7f and g).

The VS$_2$ mass loading at 45 minutes was notably higher than in the 15 and 30-minute samples, suggesting that the majority of crystal growth occurred within the first hour of the reaction. After this initial phase, the mass loading remained nearly constant for up to 20 hours (Fig. S4b†). The individual nanosheets of a microstructure gradually evolve from circular to hexagonal shapes along the *ab*-plane *via* Ostwald ripening,[22,37] as illustrated in Fig. S6.† This type of circular-to-hexagonal transformation is a time-dependent process, previously reported in the literature.[36]

XRD analysis at this stage indicated that the phase present was ammonia-intercalated VS$_2$ (VS$_2$·NH$_3$), as shown by the characteristic peaks in the 45-minute sample. As the reaction progressed to 5 hours, the peaks associated with VS$_2$·NH$_3$ (003 and 006) gradually weakened, while a new peak corresponding to the pure VS$_2$ (001) plane emerged (Fig. 8).

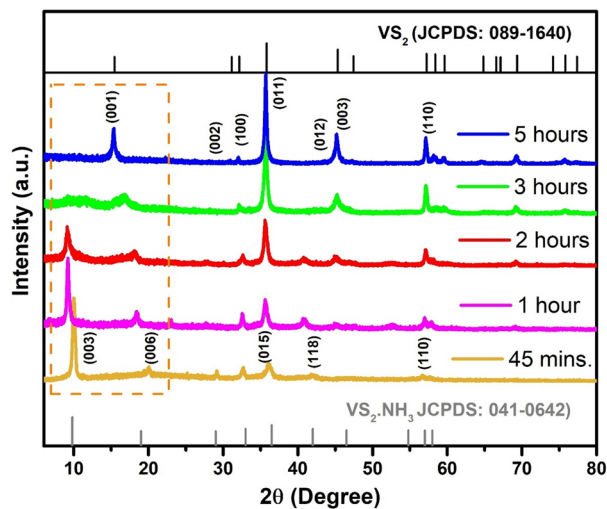**Fig. 8** XRD patterns of VS$_2$/SS hydrothermally synthesized with different reaction times (45 min, 1, 2, 3, and 5 hours).

significant role of ammonia in the early stabilization of the interlayer structure.

The DFT results also elucidate the electronic and structural changes accompanying ammonia removal. Not only does the removal reduce the interlayer distance, but it also enhances the electronic coupling between VS$_2$ layers, leading to a more thermodynamically stable structure. This is consistent with the sharp diffraction peaks observed in the XRD data, confirming the high crystallinity of the final VS$_2$ product. Integrating DFT calculations with experimental data provides a comprehensive view of the nucleation and growth process. By combining theoretical and experimental approaches, we elucidate how ammonia intercalation facilitates early-stage VS$_2$ formation and how its removal drives the formation of the layered VS$_2$ structure. This approach validates our experimental findings and also offers predictive insights into optimizing reaction parameters to control VS$_2$ morphology. SEM images further support this densification process (Fig. 6a and b), demonstrating that the removal of ammonia molecules results in the compaction of VS$_2$ nanosheets and the formation of well-defined microstructures.

Moreover, we identified well-defined hexagonal individual VS$_2$ flakes atop the thick layer of the initially synthesized hierarchical VS$_2$ microspheres (Fig. S7†). These hexagonal flakes are indicative of a spiral growth mechanism, likely driven by screw dislocations—a process observed in the literature.[38] However, unlike the idealized continuous spiral growth, the development of these flakes is periodically interrupted by dislocations along the *ab*-plane. These dislocations act as nucleation sites for the initiation of new planes, as highlighted by the dotted circles in Fig. S7.† This disruption in the spiral
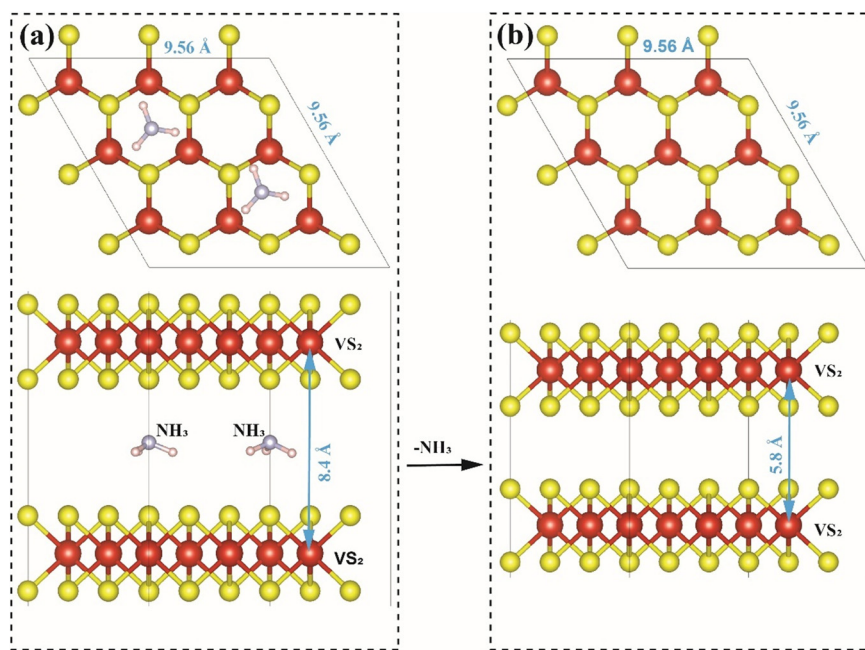
This transformation indicates that the ammonia molecules, initially trapped between VS$_2$ layers, were gradually expelled during the reaction, resulting in the formation of pure, layered VS$_2$.

Density functional theory (DFT) calculations were employed to support the experimental findings on ammonia removal and its effect on the VS$_2$ structure. Our DFT simulations revealed that the interlayer spacing decreased from 8.4 Å to 5.8 Å upon the removal of ammonia (Fig. 9), a result that closely matched the experimentally observed shift in the XRD patterns. This densification of the VS$_2$ layers, reflected in the shift of the (001) peak, underscores the

Fig. 9 Top and side view of two VS$_2$ sheets in the (a) presence and (b) absence of two intercalated ammonia molecules, indicating that the presence of ammonia increases the *d* spacing between VS$_2$ sheets.

growth path leads to the formation of additional layers, resulting in a random orientation of nanosheets.[39]

3.5 Effect of ammonia concentration

The morphology of the VS_2 microstructure was found to be highly sensitive to the amount of ammonia solution, which acts as a mineralization agent and significantly influences the quality and growth rate of the crystals.[40–42] Fig. 10(a–d) displays SEM images of VS_2/SS samples obtained after hydrothermal treatment with varying ammonia concentrations of 0, 2, 4, and 6 mL, respectively. All samples were heated at 180 °C for 10 hours. Notably, all previous experiments consistently employed 2 mL of ammonia.

By maintaining a constant volume of deionized water (30 mL) and incrementally increasing the volume of the ammonia solution from 2 to 6 mL, we observed a promotion of anisotropic growth in the VS_2 hexagonal sheets (Fig. 10b–d). Specifically, with 2 mL of ammonia, flower-like microspheres composed of hexagonal nanosheets were prominently developed (Fig. 10b). The corresponding XRD pattern aligned perfectly with the standard VS_2 spectrum (JCPDS: 89-1640), as shown in Fig. S8a.† In contrast, this flowerlike morphology was considerably suppressed when no ammonia solution (0 mL) was used. VS_2 primarily formed solid spherical balls, although some flakes were also present (Fig. 10a), possibly due to ammonia (NH_3) generated by TAA ($CH_3CSNH_2 + 2OH^- \rightarrow CHCOO^- + HS^- + NH_3$). The weaker intensity of the (001) lattice plane in the XRD pattern further indicates a reduction in the sheet-like morphology of VS_2 (Fig. S8a†).

As the ammonia concentration increased to 4 and 6 mL, the lengths and thicknesses of some hexagonal sheets further increased (Fig. 10c and d). However, low VS_2 yields were obtained for these samples, likely due to large-scale exfoliation or separation of the nanosheets promoted by ammonia, causing most of them to fall into the reaction container. The XRD patterns of these samples also showed additional peaks at 44° related to the exposed SS mesh.

Higher concentrations of NH_3 solution (4 and 6 mL) appeared to influence the exfoliation of nanosheets from the micro-flowers and promote their anisotropic growth. Ammonia is known for its significant physical and chemical activity and ability to exfoliate bulk VS_2 into ultrathin nanosheets due to its volatile nature. Conversely, the growth predominantly exhibited isotropic characteristics in the absence of ammonia. Thus, both very low and very high NH_3 concentrations negatively impacted the flowerlike morphology of VS_2. Without ammonia, VS_2 primarily formed spherical structures, while adding ammonia resulted in large, flat hexagonal crystals. This suggests that NH_3 addition promotes anisotropic growth in VS_2. Additionally, ammonia addition may be associated with changes in the pH of the solution. An exponential relationship between ammonia concentration and pH was observed, as shown in Fig. S8b.† While in the absence of NH_3 the pH was approximately 7, adding just 1 mL of ammonia raised the pH to 10.

4. Selection of optimal conditions

The synthesis of high-quality layered VS_2 nanosheets requires precise control over multiple reaction parameters to achieve the desired morphology, phase purity, and structural integrity. This study systematically investigated a broad range
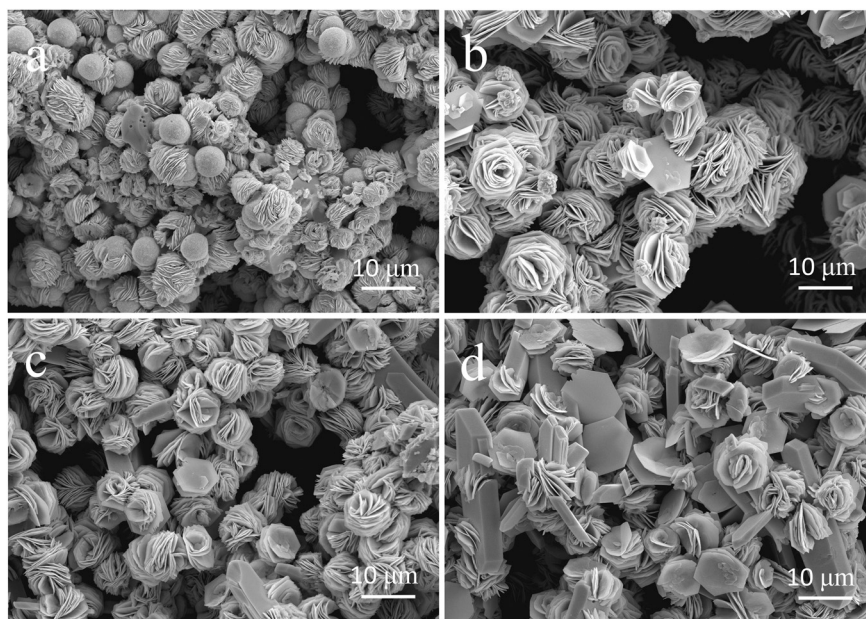

Fig. 10 (a–d) SEM micrographs of VS_2/SS synthesized by adding 0 mL, 2 mL, 4 mL, and 6 mL of ammonia solution in the reaction vessel during the hydrothermal reaction.

of reaction conditions, including precursor molar ratios, reaction time, temperature, precursor mass loadings, and ammonia concentration, while maintaining a constant solvent volume (30 mL) in a 50-mL autoclave to ensure experimental consistency. Fig. 11 summarizes the full range of investigated parameters (dashed black line) and highlights the selected synthesis conditions (red dashed line) that were exhibited to be optimal for producing well-defined layered VS_2 nanosheets. Our parametric analysis revealed the following key trends:

Precursor molar ratio: the molar ratio of $NH_4VO_3 : TAA$ strongly influenced the morphology and crystallinity of VS_2. Lower TAA concentrations led to granular and vanadium-rich phases, while higher TAA ratios promoted the formation of nanosheets with well-defined layered structures.

Reaction temperature: a broad temperature range (100–220 °C) was explored, and it was found that temperatures between 140–220 °C favored the formation of hexagonal VS_2 sheets. The most commonly reported temperature in the literature is 180 °C (Table S1†), and our experiments confirmed that this temperature yielded uniform nanosheets.

Reaction time: although 20 hours is the conventional time for hydrothermal synthesis, our study demonstrated that pure layered VS_2 nanosheets can be synthesized within 5 hours, significantly reducing reaction time without compromising structural integrity or phase purity. Growth kinetics studies indicated that VS_2 formation begins within the first 20–30 minutes as dense yarn-ball-shaped microspheres form (~5 μm in diameter) and evolve into larger microstructures (~10–12 μm) over the next 30 minutes. The transformation from ammonia-intercalated VS_2 to pure VS_2 was observed within 5 hours, making this reaction time an optimal choice.

Ammonia concentration: the amount of ammonia added to the reaction vessel significantly affected the interlayer spacing of VS_2. Controlled ammonia levels (2 ± 0.5 mL) facilitated layered nanosheet formation, whereas higher concentrations (≥4 mL) induced excessive interlayer expansion, leading to structural instability.

Precursor mass loading: a systematic increase in precursor mass loading lead to a linear increase in VS_2 yield on the substrate, with an upper limit imposed by layer adhesion and mechanical stability. Excessive loading led to thicker films, which could delaminate during handling.

We established an optimized synthesis window by integrating these experimental insights, balancing crystallinity, morphology, and process efficiency. The conditions highlighted in red in Fig. 11 denote the ideal parameters for achieving a uniform layered VS_2 nanosheet architecture, ensuring the reproducibility and scalability of the synthesis approach.

This parametric optimization serves as a practical guideline for designing VS_2-based architectures, demonstrating that reaction time can be significantly reduced to 5 hours without sacrificing nanosheet quality. These findings provide a solid foundation for future advancements in hydrothermal synthesis strategies for 2D transition metal dichalcogenides (TMDs).

5. Summary

A freestanding, porous, sponge-like vanadium disulfide (VS_2) nanosheet architecture was successfully synthesized on a stainless-steel mesh *via* a hydrothermal method. The morphology and yield of VS_2 were effectively controlled by systematically modulating key reaction parameters—including
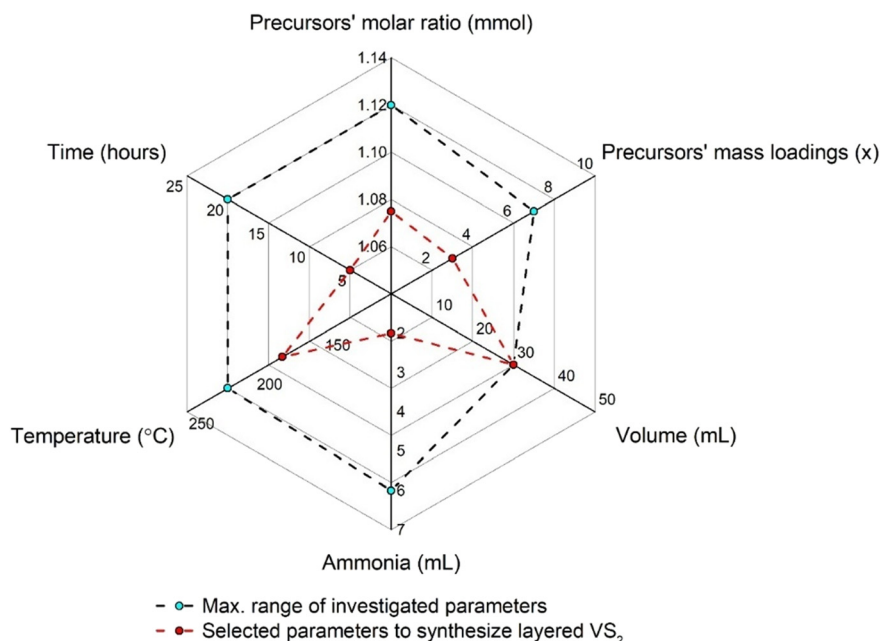

Fig. 11 Radar chart summarizing the investigated reaction parameters and the optimized conditions for layered VS_2 synthesis.

precursor molar ratios and their mass loadings, reaction time, temperature, and ammonia concentration—leading to optimized growth on a three-dimensional substrate. Our study revealed that all investigated reaction parameters had a substantial influence on the final VS_2 morphology and phase. The molar ratio of NH_4-VO_3 to TAA played a crucial role in determining the structural evolution of VS_2 nanosheets, with higher TAA concentrations (≥ 5 mmol) promoting the formation of well-defined, layered architectures, while lower concentrations resulted in granular or agglomerated morphologies. The reaction temperature was another key factor, with an optimal range identified between 140–220 °C, where hierarchical flower-like nanosheets with well-ordered hexagonal structures were obtained. Furthermore, a comparative analysis between single-step and repeated hydrothermal reaction cycles indicated that both methods followed a linear growth trend. While the single-step approach offered a time-efficient synthesis route, repeated cycles provided a strategy to achieve higher yields with lower precursor consumption. Notably, time-dependent studies demonstrated that pure VS_2 could be synthesized within 5 hours, marking a significant reduction from the conventional 20-hours reaction time. The role of ammonia concentration was also found to be critical in tailoring the morphology of VS_2. A moderate ammonia level (2 ± 0.5 mL) was essential for maintaining the layered nanosheet structure, whereas higher concentrations (≥ 4 mL) promoted anisotropic growth and interlayer expansion, leading to exfoliation and increased spacing between the sheets. Overall, this systematic parametric analysis provides new insights into optimizing hydrothermal VS_2 growth on a 3D substrate. The findings establish a strong foundation for tailoring VS_2 architectures for future applications where controlled morphology and optimized yield are crucial.

Data availability

Data will be available upon request.

Conflicts of interest

The authors declare that they have no known competing financial interests or personal relationships that could have appeared to influence the work reported in this paper.

Acknowledgements

References

1 C. Burda, X. Chen, R. Narayanan and M. A. El-Sayed, Chemistry and properties of nanocrystals of different shapes, *Chem. Rev.*, 2005, **105**, 1025–1102, DOI: **10.1021/CR030063A/ASSET/IMAGES/MEDIUM/CR030063AF00041.GIF**.

2 V. Balzani, Nanoscience and nanotechnology: The bottom-up construction of molecular devices and machines, *Pure Appl. Chem.*, 2008, **80**, 1631–1650, DOI: **10.1351/PAC200880081631/MACHINEREADABLECITATION/RIS**.

3 A. Kongkanand, K. Tvrdy, K. Takechi, M. Kuno and P. V. Kamat, Quantum dot solar cells. Tuning photoresponse through size and shape control of CdSe-TiO2 architecture, *J. Am. Chem. Soc.*, 2008, **130**, 4007–4015, DOI: **10.1021/JA0782706/SUPPL_FILE/JA0782706-FILE005.PDF**.

4 M. V. Phan, T. K. T. Tran, Q. N. Pham, M. H. Do, T. H. N. Nguyen and M. T. Nguyen, *et al.*, Controllable Synthesis of Hollow Silica Nanoparticles Using Layered Double Hydroxide Templates and Application for Thermal Insulation Coating, *ACS Omega*, 2023, **8**, 31399–31409, DOI: **10.1021/ACSOMEGA.3C03917/ASSET/IMAGES/LARGE/AO3C03917_0009.JPEG**.

5 Y. Zhu, Y. Yan, Y. Feng, Y. Liu, C. Y. Lin and Q. Ai, *et al.*, A General Synthesis Method for Covalent Organic Framework and Inorganic 2D Materials Hybrids, *Precis. Chem.*, 2024, **2**, 398–405, DOI: **10.1021/PRECHEM.3C00118/ASSET/IMAGES/LARGE/PC3C00118_0003.JPEG**.

6 X. Tian, J. Zhang, K. Rigby, D. J. Rivera, G. Gao and Y. Liu, *et al.*, Tuning Local Atomic Structures in MoS2 Based Catalysts for Electrochemical Nitrate Reduction, *Small*, 2024, 2310562, DOI: **10.1002/SMLL.202310562**.

7 S. Manzeli, D. Ovchinnikov, D. Pasquier, O. V. Yazyev and A. Kis, 2D transition metal dichalcogenides, *Nat. Rev. Mater.*, 2017, **2**(8), 1–15, DOI: **10.1038/natrevmats.2017.33**.

8 Y. Lei, T. Zhang, Y. C. Lin, T. Granzier-Nakajima, G. Bepete and D. A. Kowalczyk, *et al.*, Graphene and Beyond: Recent Advances in Two-Dimensional Materials Synthesis, Properties, and Devices, *ACS Nanosci. Au*, 2022, **2**, 450–485, DOI: **10.1021/ACSNANOSCIENCEAU.2C00017/ASSET/IMAGES/LARGE/NG2C00017_0019.JPEG**.

9 M. Chhowalla, H. S. Shin, G. Eda, L. J. Li, K. P. Loh and H. Zhang, The chemistry of two-dimensional layered transition metal dichalcogenide nanosheets, *Nat. Chem.*, 2013, **5**, 263–275, DOI: **10.1038/NCHEM.1589**.

10 J. Kang, F. Xu, C. Zhang, F. Li, O. A. Al-Hartomy and A. Al-Ghamdi, *et al.*, Vanadium Disulfide Nanosheets Synthesized by Facile Liquid-Phase Exfoliation for Ammonia Detection with High Selectivity, *Adv. Electron. Mater.*, 2022, **8**, 2100567, DOI: **10.1002/AELM.202100567**.

11 A. K. Patel, P. K. Vishwakarma, R. Giri and A. Srivastava, Vanadium disulfide nanosheets based membrane for filter application, *J. Taiwan Inst. Chem. Eng.*, 2024, **161**, 105483, DOI: **10.1016/J.JTICE.2024.105483**.

12 Y. Dong, Y. Liu, Y. Hu, K. Ma, H. Jiang and C. Li, Boosting reaction kinetics and reversibility in Mott-Schottky VS_2/MoS_2 heterojunctions for enhanced lithium storage, *Sci. Bull.*, 2020, **65**, 1470–1478, DOI: **10.1016/j.scib.2020.05.007**.

13 D. Sahoo, S. Senapati and R. Naik, Progress and prospects of 2D VS_2 transition metal dichalcogenides, *FlatChem*, 2022, **36**, 100455, DOI: **10.1016/J.FLATC.2022.100455**.

14 M. Liu, Z. Zhao, W. Zhang and W. Zheng, Perspective of Vanadium Disulfide: A Rising Star Finds Plenty of Room in Single and Multielectron Energy Storage, *Energy Fuels*, 2022, **36**, 13931–13955, DOI: **10.1021/ACS.ENERGYFUELS.2C02642/ ASSET/IMAGES/MEDIUM/EF2C02642_0013.GIF**.

15 W. Li, H. M. Kheimeh Sari and X. Li, Emerging Layered Metallic Vanadium Disulfide for Rechargeable Metal-Ion Batteries: Progress and Opportunities, *ChemSusChem*, 2020, **13**, 1172–1202, DOI: **10.1002/CSSC.201903081**.

16 L. Li, Z. Li, A. Yoshimura, C. Sun, T. Wang and Y. Chen, *et al.*, Vanadium disulfide flakes with nanolayered titanium disulfide coating as cathode materials in lithium-ion batteries, *Nat. Commun.*, 2019, **10**, 1–10, DOI: **10.1038/ s41467-019-09400-w**.

17 Q. Ji, C. Li, J. Wang, J. Niu, Y. Gong and Z. Zhang, *et al.*, Metallic Vanadium Disulfide Nanosheets as a Platform Material for Multifunctional Electrode Applications, *Nano Lett.*, 2017, **17**, 4908–4916, DOI: **10.1021/ACS.NANOLETT.7B01914**.

18 J. H. Han, M. Kwak, Y. Kim and J. Cheon, Recent Advances in the Solution-Based Preparation of Two-Dimensional Layered Transition Metal Chalcogenide Nanostructures, *Chem. Rev.*, 2018, **118**, 6151–6188, DOI: **10.1021/ACS.CHEMREV.8B00264/ ASSET/IMAGES/LARGE/CR-2018-00264S_0034.JPEG**.

19 J. Li, Q. Wu and J. Wu, Synthesis of Nanoparticles via Solvothermal and Hydrothermal Methods, *Handbook of Nanoparticles*, 2015, pp. 1–28, DOI: **10.1007/978-3-319-13188- 7_17-1**.

20 M. Nasilowski, B. Mahler, E. Lhuillier, S. Ithurria and B. Dubertret, Two-Dimensional Colloidal Nanocrystals, *Chem. Rev.*, 2016, **116**, 10934–10982, DOI: **10.1021/ACS.CHEMREV.6B00164/ ASSET/IMAGES/MEDIUM/CR-2016-00164J_0035.GIF**.

21 C. S. Rout, R. Khare, R. V. Kashid, D. S. Joag, M. A. More and N. A. Lanzillo, *et al.*, Metallic Few-Layer Flowerlike VS$_2$ Nanosheets as Field Emitters, *Eur. J. Inorg. Chem.*, 2014, **2014**, 5331–5336, DOI: **10.1002/EJIC.201402448**.

22 J. Z. Liu and P. F. Guo, VS$_2$ nanosheets: A potential anode material for lithium batteries, *J. Inorg. Mater.*, 2015, **30**, 1339–1344, DOI: **10.15541/JIM20150345**.

23 J. Fang, W. Shen, S. H. S. Cheng, S. Ghashghaie, H. K. Shahzad and C. Y. Chung, Four-electrode symmetric setup for electrochemical impedance spectroscopy study of Lithium–Sulfur batteries, *J. Power Sources*, 2019, **441**, 227202, DOI: **10.1016/J.JPOWSOUR.2019.227202**.

24 S. Ghashghaie, S. H. S. Cheng, J. Fang, H. K. Shahzad, R. L. W. Ma and C. Y. Chung, Electrophoretically deposited binder-free 3-D carbon/sulfur nanocomposite cathode for high-performance Li–S batteries, *J. Energy Chem.*, 2020, **48**, 92–101, DOI: **10.1016/j.jechem.2019.12.015**.

25 S. Ghashghaie, S. H. S. Cheng, J. Fang, H. K. Shahzad, G. Muhyodin and H. Liu, *et al.*, Unique flake-shaped sulfur morphology favored by the binder-free electrophoretically deposited TiO$_2$ layer as a promising cathode structure for Li-S batteries, *J. Alloys Compd.*, 2024, **1009**, 176907, DOI: **10.1016/J.JALLCOM.2024.176907**.

26 M. Tamtaji, S. Kwon, C. B. Musgrave, W. A. Goddard and G. Chen, Reaction Mechanism of Rapid CO Electroreduction to Propylene and Cyclopropane (C3$^+$) over Triple Atom, *Catalysts*, 2024, **16**(38), 50027–51782, DOI: **10.1021/ acsami.4c06257**.

27 M. Tamtaji, M. G. Kim, J. Wang, P. R. Galligan, H. Zhu and F. Hung, *et al.*, A High-Entropy Single-Atom Catalyst Toward Oxygen Reduction Reaction in Acidic and Alkaline Conditions, *Adv. Sci.*, 2024, 2309883, DOI: **10.1002/advs.202309883**.

28 M. Tamtaji, S. Cai, W. Wu, T. Liu, Z. Li and H. Y. Chang, *et al.*, Single and dual metal atom catalysts for enhanced singlet oxygen generation and oxygen reduction reaction, *J. Mater. Chem. A*, 2023, **11**, 7513–7525, DOI: **10.1039/ d2ta08240c**.

29 X. Zhu, W. Zhao, Y. Song, Q. Li, F. Ding and J. Sun, *et al.*, In Situ Assembly of 2D Conductive Vanadium Disulfide with Graphene as a High-Sulfur-Loading Host for Lithium–Sulfur Batteries, *Adv. Energy Mater.*, 2018, **8**, 1–9, DOI: **10.1002/ aenm.201800201**.

30 X. Zhang, Q. He, X. Xu, T. Xiong, Z. Xiao and J. Meng, *et al.*, Insights into the Storage Mechanism of Layered VS$_2$ Cathode in Alkali Metal-Ion Batteries, *Adv. Energy Mater.*, 2020, **10**, 1904118, DOI: **10.1002/AENM.201904118**.

31 M. Zhong, Y. Li, Q. Xia, X. Meng, F. Wu and J. Li, Ferromagnetism in VS$_2$ nanostructures: Nanoflowers versus ultrathin nanosheets, *Mater. Lett.*, 2014, **124**, 282–285, DOI: **10.1016/J.MATLET.2014.03.110**.

32 X. Chen, K. Yu, Y. Shen, Y. Feng and Z. Zhu, Synergistic Effect of MoS$_2$ Nanosheets and VS$_2$ for the Hydrogen Evolution Reaction with Enhanced Humidity-Sensing Performance, *ACS Appl. Mater. Interfaces*, 2017, **9**, 42139–42148, DOI: **10.1021/ACSAMI.7B14957**.

33 W. Li, J. Huang, L. Feng, L. Cao, Y. Feng and H. Wang, *et al.*, Facile in situ synthesis of crystalline VOOH-coated VS$_2$ microflowers with superior sodium storage performance, *J. Mater. Chem. A*, 2017, **5**, 20217–20227, DOI: **10.1039/ C7TA05205G**.

34 D. Meier, R. Ragunathan, S. Degener, A. Liehr, M. Vollmer and T. Niendorf, *et al.*, Reconstruction of incomplete X-ray diffraction pole figures of oligocrystalline materials using deep learning, *Sci. Rep.*, 2023, **13**, 1–12, DOI: **10.1038/s41598- 023-31580-1**.

35 T. Jiao, Q. Yang, S. Wu, Z. Wang, D. Chen and D. Shen, *et al.*, Binder-free hierarchical VS$_2$ electrodes for high-performance aqueous Zn ion batteries towards commercial level mass loading, *J. Mater. Chem. A*, 2019, **7**, 16330–16338, DOI: **10.1039/C9TA04798K**.

36 J. Wang, S. Yi, J. Liu, S. Sun, Y. Liu and D. Yang, *et al.*, Suppressing the Shuttle Effect and Dendrite Growth in Lithium-Sulfur Batteries, *ACS Nano*, 2020, **14**, 9819–9831, DOI: **10.1021/acsnano.0c02241**.

37 P. W. Voorhees, The theory of Ostwald ripening, *J. Stat. Phys.*, 1985, **38**, 231–252, DOI: **10.1007/BF01017860**.

38 D. Zhang, H. Zhang, J. Cheng, H. Raza, T. Liu and B. Liu, *et al.*, Customizing coaxial stacking VS2 nanosheets for dual-band microwave absorption with superior performance in the C- And Ku-bands, *J. Mater. Chem. C*, 2020, **8**, 5923–5933, DOI: **10.1039/D0TC00763C**.

39 Z. Fang, S. Hao, L. Long, H. Fang, T. Qiang and Y. Song, The enhanced photoelectrochemical response of SnSe$_2$ nanosheets, *CrystEngComm*, 2014, **16**, 2404–2410, DOI: **10.1039/C3CE42082E**.

40 K. Suchanek, M. Perzanowski, J. Lekki, M. Strąg and M. Marszałek, Ammonium Hydroxide Mediated Hydrothermal Crystallization of Hydroxyapatite Coatings on Titanium Substrate, *Ceramics*, 2019, **2**, 180–189, DOI: **10.3390/CERAMICS2010016**.

41 X. Yu, H. Wang, Y. Liu, X. Zhou, B. Li and L. Xin, *et al.*, One-step ammonia hydrothermal synthesis of single crystal anatase TiO$_2$ nanowires for highly efficient dye -sensitized solar cells, *J. Mater. Chem. A*, 2013, **1**, 2110–2117, DOI: **10.1039/C2TA00494A**.

42 G. Yang and S. J. Park, Conventional and Microwave Hydrothermal Synthesis and Application of Functional Materials: A Review, *Materials*, 2019, **12**, 1177, DOI: **10.3390/MA12071177**.